SOILS, SEC 3 • REMEDIATION AND MANAGEMENT OF CONTAMINATED
OR DEGRADED LANDS • RESEARCH ARTICLE

Soil redox maps: assessment of small field-scale redox zonation by Mn and Fe oxide-coated IRIS films

Kristof Dorau[1,2] · Theresa Zanger[1] · Andreas Bolten[1] · Tim Mansfeldt[1]

Abstract

Purpose Intra-field redox zonation across depth in soils can be heterogeneous and account for the presence of biogeochemical "hot spots." Understanding the spatial distribution of hot spots is desirable but hard to obtain.

Materials and methods In this study, low-cost manganese (Mn) and iron (Fe) oxide-coated Indicator of Reduction In Soils (IRIS) films were installed at a wetland. A grid soil sampling approach within a monitoring plot (20×20 m; 2-m raster cells) featured a microrelief of 29 cm above the water table (WT). Data of Mn and Fe oxide removal along IRIS films and natural (newly formed) Fe oxides along Mn IRIS served to spatially resolve digital redox maps by ordinary kriging.

Results and discussion A distinctive redox zonation due to the microrelief could be differentiated with the lowest oxide loss at elevated terrain. Located at 9 to 29 cm above the WT, small-scaled pattern of oxide loss of a few cm^2 occurred due to anoxic microsites (zone I). Zone II was located at 4 to 9 cm above the WT (Fe^{2+} sink), whereas zone III extended below and a few cm above the WT (Fe^{2+} source). Mn IRIS displayed three times more oxide loss, compared to Fe IRIS. Thereupon, natural Fe oxides formed to a major extent along Mn IRIS with on average 80% in redox zone I and II. Thus, Fe^{2+} was an omnipresent constituent in soil solution, while no or only minor synthetic Fe oxide along Fe IRIS were removed. This highlights the clear difference between the reducibility of pedogenic Fe oxides and synthetic Fe oxides. Overall, the large reactive surface area of IRIS can circumvent problems associated with misclassification of the soil redox status using redox electrodes, which are more susceptible to soil spatial variability.

Conclusions Homogeneity and representativeness of redox sensitive topsoil samples or soil solutions can in fact only be guaranteed within a range < 5 m for this particular study site. IRIS can be utilized to investigate both: microsite-driven features such as neo-formed natural Fe oxides along Mn IRIS (< mm to cm scale) and geo-referenced oxide loss from IRIS at the plot scale (tens to hundreds of meters). Soil redox maps deliver important spatial information for the worldwide growing demand for high-resolution digital soil maps.

Keywords Environmental monitoring · IRIS · Kriging · Microrelief · Redox processes · Soil reducing conditions

✉ Kristof Dorau
  K.Dorau@uni-koeln.de; Kristof.Dorau@bgr.de

1   Faculty of Mathematics and Natural Sciences, Department of Geosciences, Institute of Geography, University of Cologne, Albertus-Magnus-Platz, 50923 Cologne, Germany

2   Federal Institute for Geosciences and Natural Resources (BGR), Stilleweg 2, 30655 Hannover, Germany

1 Introduction

Characterization of the soil redox status as a driver of biogeochemical processes is outstanding to account for trace metal solubility or greenhouse gas emissions, but the complex interplay of physical, chemical, and biological constrained conditions makes it particularly challenging to infer these conditions across various scales. The onset of reducing conditions is typically related to soils that are temporarily (weeks to months) or permanently water saturated in wetlands with low elevation featuring near-surface groundwater (Ponnamperuma 1972; Reddy and DeLaune 2008) but can also occur due to perched water tables and stagnant water in terrestrial upland

soils (Dorau et al. 2020). Flooding and an increase in soil water content hampers the replenishment of oxygen (O_2) with reduced O_2 diffusion rates slowed-down $3 \cdot 10^5$ times (Rohe et al. 2021; Zausig et al. 1993). Thus, air-filled pores (ε) and the connected air-filled porosity (ε_{conn}) are critical parameters to assess aeration processes in soils but are highly variable in space and time (Dorau et al. 2021). Thereupon, other intrinsic soil physical (e.g., bulk density, aggregation), chemical (e.g., pH, soil organic matter content and composition), and biological properties (e.g., microbial community and abundance) impact the reduction (or oxidation) intensity—expressed as redox potential (E_H) in units of electrochemical energy (mV; DeLaune and Reddy 2005). The aforementioned parameters will ultimately change when a soil is transferred to the laboratory because the E_H will change immediately after retrieval of the sample, due to aeration of a previously reducing soil environment when exposed to O_2. Microcosm experiments certainly have a great value because redox conditions can be strictly defined by flushing either O_2 (E_H increase) or N_2 (E_H decrease) into the incubation system to investigate trace element solubility (Hindersmann and Mansfeldt 2014) or the release of greenhouse gases (Yu and Patrick 2004). However, these experiments cannot compensate the importance of soil architecture—it is the spatial arrangement of the pore space and solid phase that determines physical, chemical, and biological processes (Vogel et al. 2022). Characterization of the soil redox status in the laboratory is possible by using undisturbed samples within a steel cylinder of 250 cm^3 sample volume (Dorau et al. 2018a), larger sample volume of 2,000 cm^3 using the redoxtron incubation system made of acryl glass housing (Dorau et al. 2023), or using even larger profiling column experiments up to 22,000 cm^3 (Schroeder et al. 2017). The non-destructive nature of these experiments has advantages but cannot imitate intra-field variability due to (i) variable soil properties occurring at small spatial scale with impact on the soil redox status or (ii) changes in the microrelief with impact on capillary rise from shallow groundwater. Thus, uncertainties arise how unique or general results from single sampling sites and laboratory incubation experiments are in comparison with real-world scenarios occurring under field conditions. Overall, redox processes and therefore soils must be studied in their natural state with as little disturbance as possible. Thus, continuous in situ monitoring of E_H by permanently installed redox electrodes is of utmost importance in linking environmental conditions to the soil redox status and vice versa (Dorau and Mansfeldt 2016a).

Determination of the soil redox status by redox electrodes has many advantages but thermodynamic restrictions (Whitfield 1974). The microsite dependent measurement and high standard deviation between replicates with associated high costs for the data logging equipment are certainly further disadvantages. As a result, a spatiotemporal characterization of the soil redox status and

the relationship with physicochemical properties at the field-scale is missing at present. As an alternative to E_H measurements, Indicator of Reduction In Soil (IRIS) tools gained attention since nearly two decades and are simple field methods to assess and sometimes monitor soil reducing conditions (Sapkota et al. 2022). White polymer surfaces are coated either with laboratory-made suspensions of manganese (Mn) (Dorau and Mansfeldt 2015; Stiles et al. 2010) or iron (Fe) oxyhydroxides (Jenkinson and Franzmeier 2006; Rabenhorst and Burch 2006). Under dissimilatory reductive dissolution of the oxide coating, the visibility of the white polymer surface serves as a proxy to differentiate weakly (E_H 300 to 100 mV at pH 7; tri- and tetravalent Mn is consumed) and moderately reducing soil conditions ($E_H < 100$ mV at pH 7; trivalent Fe is consumed) according to the sequential reduction sequence (Dorau and Mansfeldt 2015). Mn IRIS have sometimes advantages compared with Fe IRIS because short-term monitoring on a daily basis is possible and oxide removal occurs even at soil temperatures as low as 5 °C (Dorau et al. 2018b; Rabenhorst et al. 2021), which would be beneficial in areas where temperatures are consistently low (Schwyter 2020). The onset of weakly reducing conditions with preferential Mn oxide removal over Fe oxide removal from IRIS tools appeared to be especially feasible in capillary fringes (CF) above the water table (WT), where soil pores are not fully water saturated but soil water content is close to water saturation (Dorau et al. 2016). Thus, a microrelief with an unconfined aquifer, i.e., where the WT is at equilibrium with atmospheric pressure, should separate hot spots in the field where Mn and Fe oxide removal is distinctively different. IRIS are commonly attained to differentiate between study sites or substrates by a nested sampling approach (summarized in Sapkota et al. 2022). However, in order to differentiate decisive redox zones at the plot scale, a grid soil sampling approach with a larger number of IRIS is mandatory. Such a high-spatial field analysis of Mn and Fe oxide mineral (trans)formation along IRIS has not been investigated at present.

In this study, a grid soil sampling approach (20 × 20 m monitoring site with 2-m raster cells) has been conducted. Two Mn and two Fe oxide-coated IRIS (10-cm coated film length) were simultaneously installed per sampling point. In total, 200 Mn and 200 Fe IRIS films were installed for a one-month period and oxide loss analyzed by sophisticated image analysis. Data of oxide loss and mineral transformation served as a base to construct by ordinary kriging high-resolution digital maps of the soil redox status. The ultimate objectives of this work were to (i) assess the impact of the microrelief (29-cm differences in altitude above the water table) on the spatial distribution of soil reducing conditions and (ii) account for the spatial dependence of mineral (trans)formation by IRIS

using semivariograms and relate these to other soil properties at the field scale.

2 Materials and methods

2.1 Study site and sampling design

Soil sampling and monitoring of the soil redox status were conducted in the district of Recklinghausen, Germany (51° 48′ 59″ N, 7° 12′ 59″ E). A deep layer of > 50-m Upper Cretaceous sand forms the local aquifer and this is overlain by a thin coverage (< 3 m) of Quaternary sand and marly ground moraine deposited during the Saale glaciation (Banning et al. 2009; Mansfeldt and Overesch 2013). The study site is morphologically relatively flat with altitudes of about 50 m above sea level (asl), but glaciofluvial processes resulted in a microrelief with an absolute difference in altitude of 29 cm from 46.75 to 47.04 m asl for the monitoring site under investigation. Water table depths are generally low (< 1 m) in this lowland area, which favors a separation into elevated "drier" sites and "flooded" sites in lower terrain rendering this study site very suitable for the planned investigations. With decreasing altitude, the soil catena typically consist of the order Haplic Gleysol (Petrogleyic), Haplic Gleysol (Hyperhumic), and Mollic Gleysol due to the subtle variations in the soil hydrologic regime and thereupon altered pathways of soil formation. More detailed information about the study site can be found in Mansfeldt and Overesch (2013) and Dorau et al. (2016). We employed a grid soil sampling approach, and the boundary for the monitoring site was 20 × 20 m with 2-m raster cells (Fig. S1). At each of the individual 100 sampling points, a Pürckhauer auger was drilled four times into the soil down to 10-cm soil depth (2.1 cm Ø = ~ 40 cm^3 soil volume). The excavated four soil samples were merged to obtain a representative mixed sample per sampling plot, which yielded a total of 50 to 120-g sample weight.

2.2 Soil properties

The disturbed soil samples were oven dried at 40 °C, sieved < 2 mm and partly milled (MM400, Retsch, Haan, Germany) to measure the following soil physicochemical properties: Soil pH was measured potentiometrically within a 0.01 M $CaCl_2$ solution mixed 5:1 with soil (v/v) and soil organic carbon (SOC) by dry combustion with a CNS analyzer (vario EL cube, Elementar, Hanau, Germany). For the X-ray fluorescence spectrometry (XRF), we pressed pellets from 5 g pulverized soil sample mixed with 1 g of CEREOX binding agent, which were subsequently measured by using a XRF analyzer (XEPOS,

Spectro, Kleve, Germany). The pellets were used to measure total Fe content.

2.3 Manufacturing and installation of IRIS films

Mn IRIS consists of a coating made of birnessite according to Dorau and Mansfeldt (2015) with slight modifications in the permanganate to lactate ratio Rabenhorst and Persing (2017). The coating of Fe IRIS is composed of a ferrihydrite and goethite ratio (Rabenhorst and Burch 2006). To validate the ratio between ferrihydrite and goethite, we used acid-oxalate extraction (Fe_{ox}; Schwertmann 1964) to extract ferrihydrite and dithionite-citrate-bicarbonate (Fe_{DCB}; Mehra and Jackson 1960) extraction to extract the total Fe content from the polymer surface. Fe IRIS for our experiment yielded a Fe_{ox}/Fe_{DCB} ratio of 0.72, indicating that the major fraction was short-range ordered being ferrihydrite. The polymer surface for the Mn and Fe oxide coating were thin PVC films that enable ease and flexibility in terms of installation and image analysis (Rabenhorst 2018). The films were 7.5 cm in width and 15 cm in length with the lower 10 cm coated either with synthetic Mn or Fe oxides. The rationale for choosing a coated IRIS film length of 10 cm takes into account German soil legislation methods. Within this document, a sampling depth of 10 cm is recommended if risk assessment on the transfer pathway soil to plant with pasture as usage is considered (BBodSchV 1999). For deployment, each film was rolled smaller than 2 cm Ø to fit into the pre-drilled pilot holes (Rabenhorst 2018) in duplicate per sampling point to achieve a total of 200 Mn IRIS and 200 Fe IRIS. Incubation of the films lasted for a one-month period in spring (from 2022–03-10 to 2022–04-10). During this time, groundwater tables are typically close to the soil surface, and soil temperature is rising, thus stimulating microbial activity in the topsoil and favoring oxide removal along IRIS films. Daily air temperature and precipitation data were taken from the closest meteorological station operated by the German Meteorological Service in Lüdinghausen-Brochtrup.

2.4 Image analysis procedure

After retrieval of the films, adhering soil was gently rinsed off in the field with deionized water, and the films were allowed to air dry. Afterwards, all films were scanned in the lab (ScanSnap iX100, Fujitsu, Tokio, Japan) to further analyze the digitalized images. The workflow to analyze and quantify mineral (trans)formation was performed within R (version 4.2.0). The script builds upon the package imager (Barthelme 2021) and multiple packages from the Tidyverse (Wickham et al. 2019) with the following steps: First, the images were converted from RGB towards grayscale, and subsequently a binary image was created using automatic thresholding. Automatic image analysis is robust and

independent of human intuition but only successful if the pixel values have a clear bimodal distribution between the objects and the background, e.g., to inspect and quantify areas along the film were a change of the original oxide coating were apparent. In 70% of the cases, automatic computation by kmeans method was successful without further adjustment. However, in the other 30% of the examples, the threshold must be adapted to match visually best the depletion patterns along the films. By default, the function imager::threshold() function has an adjust function with a default value of 1. Very bright images, e.g., due to the appearance of the white PVC underneath the oxide coating, had to be adjusted with values between 0.8 and 0.9, whereas dark images with only minor oxide loss had to be adjusted between 1.3 and 1.5. This was equally true for Mn and Fe IRIS films to match best the visual inspection by eye. Exclusively for Mn IRIS films, brownish precipitates of natural Fe oxides were individually analyzed because these zones feature a special characteristic by a non-enzymatic abiotic reaction of the synthetic Mn oxide coating with Fe^{2+} from soil solution (Dorau and Mansfeldt 2015; Dorau and Mansfeldt 2016a, b). Examples can be seen in the supporting information (Fig. S2). Thus, by defining category specific thresholds corresponding to colors and summing pixels assigned to these colors divided by the total number of pixels from each film, we yielded the final categories to construct redox maps as following with the units oxide change in % for Mn IRIS with the following:

(i) Total Mn oxide loss including natural Fe oxide precipitates and areas where neither Mn nor Fe oxides were visible.

(ii) Natural Fe oxide precipitates.

(iii) Areas with only the white PVC.
For Fe IRIS, oxide loss was quantified for the following:

(iv) Areas with partial and complete oxide loss of the synthetic Fe oxide coating.

2.5 Digital elevation model and geostatistical computations

All sampling points were surveyed by measuring the UTM coordinates and the absolute height in m asl with a differential GPS system (Hiper V, Topcon, Tokio, Japan). We utilized the German Combined Quasigeoid Model (GCG2016) to obtain a lateral and vertical measurement accuracy with a resolution of 0.5 to 1 cm. All data was processed in RStudio primarily upon the packages sf (Pebesma 2018) and gstat (Gräler et al. 2016) to handle the spatial data and automap (Hiemstra et al. 2009) for the kriging procedure. First, the data were analyzed by descriptive methods, which revealed that SOC content

and the information from oxide removal of the Mn and Fe IRIS featured a skewness. Thereupon natural logarithmic transformation of the data was performed to obtain a normal distribution. The correlation of the parameters was calculated by Pearson's correlation coefficient. Semivariograms were calculated in order to determine the degree of spatial variability with a lag distance of 2 m and fitting of a spherical model. We applied two-dimensional ordinary kriging (OK) to interpolate the values for the maps. Leave-one-out method was applied for cross validation between the predicted values from OK and the original data (Kaur and Rishi 2018). This cross-validation method makes a prediction from a single observation of the original sample size (testing data), while no predictions are made from the remaining observations (training data). This process was iterated across all of the observations using the inbuilt wizard inside ArcGIS instead of RStudio. Model validation of the interpolation procedure included, first, the average standard error (ASE) as follows:

$$ASE = \sqrt{\frac{\sum_{i=1}^{n} \sigma^2(s_i)}{n}} \tag{1}$$

where s_i as the locations of the samples, $\sigma^2(s_i)$ as the standard measurement error at the ith location, and n is the sample size. Second, the root mean square error (RMSE) is calculated as follows:

$$RMSE = \sqrt{\frac{\sum_{i=1}^{n} [\hat{z}(s_i) - z(s_i)]^2}{n}} \tag{2}$$

where $z(s_i)$ is the associated value at the location of the samples and $\hat{z}(s_i)$ is the predicted or interpolated value by OK. Third, the dimensionless RMSE called scatter index (SI; in %) as follows:

$$SI = \frac{RMSE}{\overline{Z}} * 100 \tag{3}$$

where $\overline{Z}$ as the mean of the observations at each grid point. The ASE values should be as small as possible and signify the goodness of the prediction model with RMSE determining the error size ("prediction error"). ASE close to the RMSE indicates that prediction errors are correctly assessed, ASE > RMSE indicates that the variability of prediction is overestimated, and ASE < RMSE indicates that the variability of prediction is underestimated (Kaur and Rishi 2018). All values should be as small as possible with values close to zero indicating a perfect fit to very high values indicating a poor fit (Kisi et al. 2013).

3 Results

3.1 Meteorological conditions, soil properties, and redox maps

The mean air temperature during the film installation was 7.45 ± 2.65 °C but was considerably lower with 4.81 ± 2.29 °C during the previous two-month period (Fig. S3). Due to the higher heating capacity of soil compared with air, it seems reasonable to state that soil temperature was on average < 5 °C with minor daily exceptions towards the end of the monitoring period. Precipitation was marginal during the first three weeks of the IRIS installation period with 7.3 mm but pronounced towards the fourth and final week with 63 mm. Overall, the microrelief clearly favored a separation with an overall height difference of 29 cm from the lowest altitude in the south eastern part (46.75 m asl) and the highest altitude in the north western part (47.04 m asl) (Fig. 1A). At the lowest located sampling points, ponding conditions of 1 cm occurred that visualizes and clearly identifies the position of the WT rendering

the extent of the capillary fringe (unsaturated or vadose zone) of up to 28 cm above the WT towards the highest altitude (Fig. 1A and Fig. S4). Although we have no in situ data about soil water content, we assume that field capacity was reached for sampling points approximately 15 cm above the water table because no water dripped out of the auger during sampling. However, quick condensation of water inside the airtight plastic bag directly after removal of the soil sample indicates high water contents.

A strongly acidic soil milieu is characteristic for the study site with on average pH 4.6 ± 02 (Fig. 1B), elevated SOC content of 86 ± 26 g kg^{-1} (Fig. 1C), and 94 ± 23 g kg^{-1} Fe content (Fig. 1D). The altitude was negatively correlated with SOC content being highest at the lowest terrain ($r = -0.67$**) but with lower r values for pH and Fe content (Table 1). Data about oxide removal from Mn and Fe IRIS were also significantly negatively related with altitude with the highest oxide removal occurring in the south eastern part at the study site (Table 1). Whereas up to 100% oxide removal occurred for Mn IRIS with on average 38 ± 31%, the total depleted area for Fe IRIS
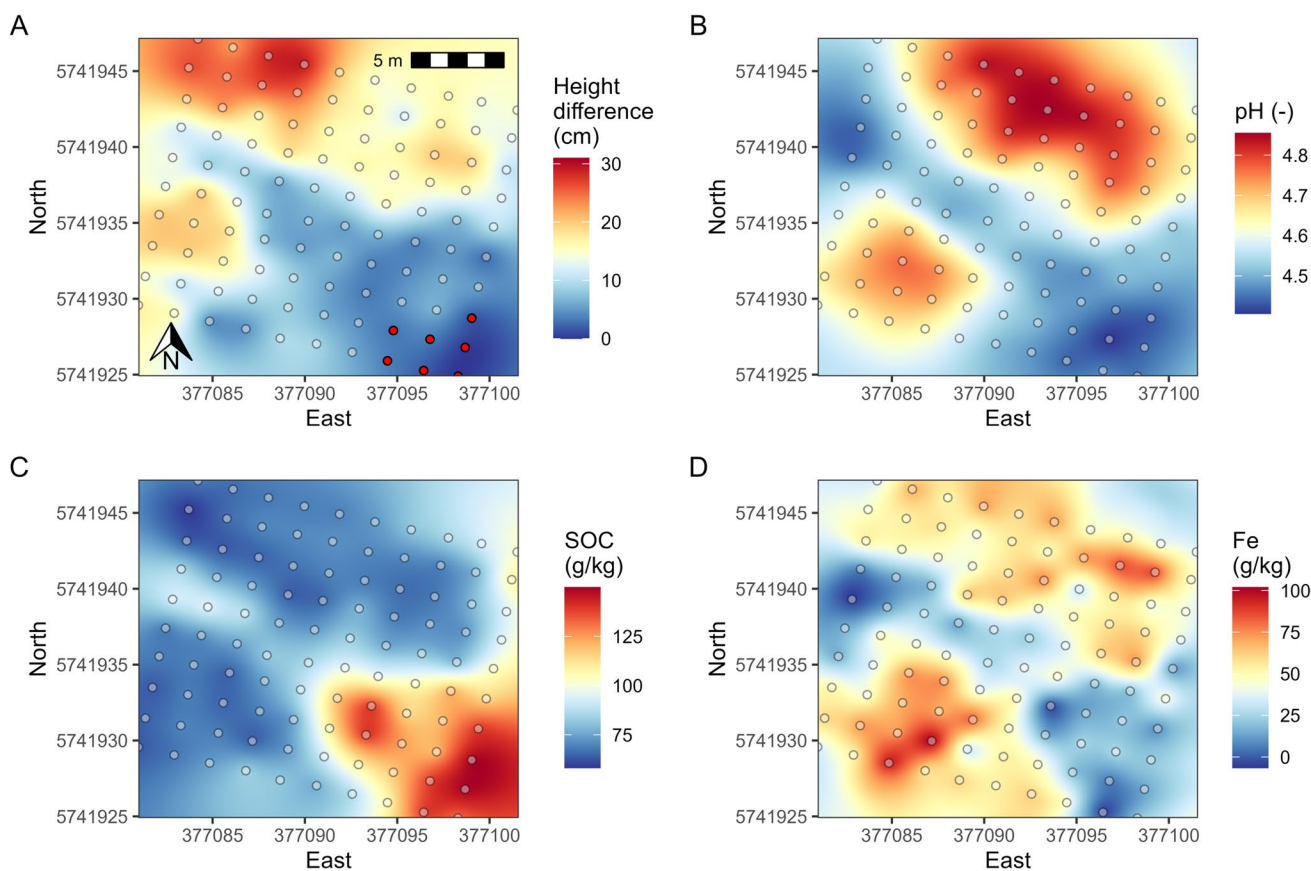
Fig. 1 Interpolated maps by ordinary kriging for altitude (**A** from 46.746 to 47.040 m asl), pH (**B** 0.01 M CaCl$_2$), soil organic carbon (**C** SOC), and total Fe content (**D**) for the study site. The sampling points in red in (**A**) featured ponding conditions of 1 cm during installation and retrieval of the IRIS films

**Table 1** Correlation matrix for the spatial information analyzed at the monitoring site ($n = 100$)

Parameters	Altitude	SOC	pH	Fe content	Fe oxide removal (Fe IRIS)	Mn oxide removal (Mn IRIS)	Natural Fe oxides (Mn IRIS)
Units	(m asl)	(g kg^{-1})	(-)	(g kg^{-1})	(%)	(%)	(%)
Altitude	1						
SOC	− 0.67**	1					
pH	0.39*	− 0.44**	1				
Fe content	0.32*	− 0.61**	0.63**	1			
Fe oxide removal (Fe IRIS)	− 0.70***	0.79***	− 0.38**	− 0.48**	1		
Mn oxide removal (Mn IRIS)	− 0.78***	0.81***	− 0.39**	− 0.50**	0.94***	1	
Natural Fe oxides (Mn IRIS)	− 0.62**	0.38*	− 0.30*	− 0.23	0.41*	0.59**	1

$^*p<0.05$; $^{**}p<0.01$; $^{***}p<0.001$

was at maximum 83% and threefold less with on average 13 ± 21% (Fig. 2). The spatial extent of enhanced Mn oxide loss of Mn IRIS matched with areas of predominant Fe oxide loss of Fe IRIS (Fig. 2A and B). Natural Fe oxides formed to a significant extent along Mn IRIS with a maximum of 92% and on average 27 ± 22%. Interestingly, these localized hot spots of natural Fe oxides were not exclusively at the lowest altitude but formed a rim situated between the lowest and the highest altitude (Fig. 2C).

3.2 Redox zonation and depletion patterns from IRIS films

A clear trend is apparent that the microrelief has an impact on oxide removal for Mn and Fe IRIS (Fig. 3A). Whereas for Mn IRIS a steadily and more linear relationship with altitude exists, Fe IRIS appear to have a tipping point between very minor (<5% oxide removal) on the one hand and more oxide loss below a certain threshold, i.e., the isoline or contour line at a certain altitude. We differentiated based upon the trend
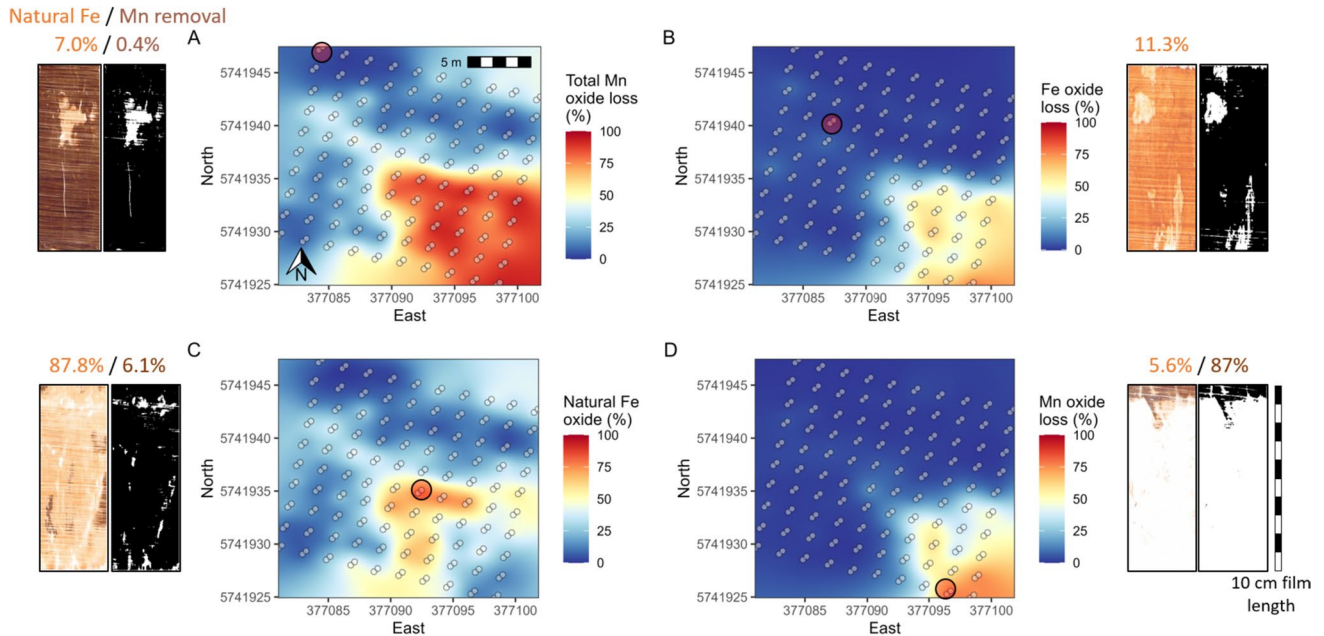
Fig. 2 Interpolated redox maps for total Mn oxide removal from Mn films (**A**) and for total Fe oxide removal from Fe films (**B**). Exclusive for Mn films, Mn oxide loss is differentiated for the percentage area along the films where natural Fe oxides precipitated (**C**) and for complete oxide loss where neither natural Fe oxide nor Mn oxide remained along the film surface (**D**). The red dot in each panel (**A** to **D**) is the position with an example for a Mn (**A**, **C**, **D**) and Fe film (**B**) along with the binarized image after thresholding (left and right)
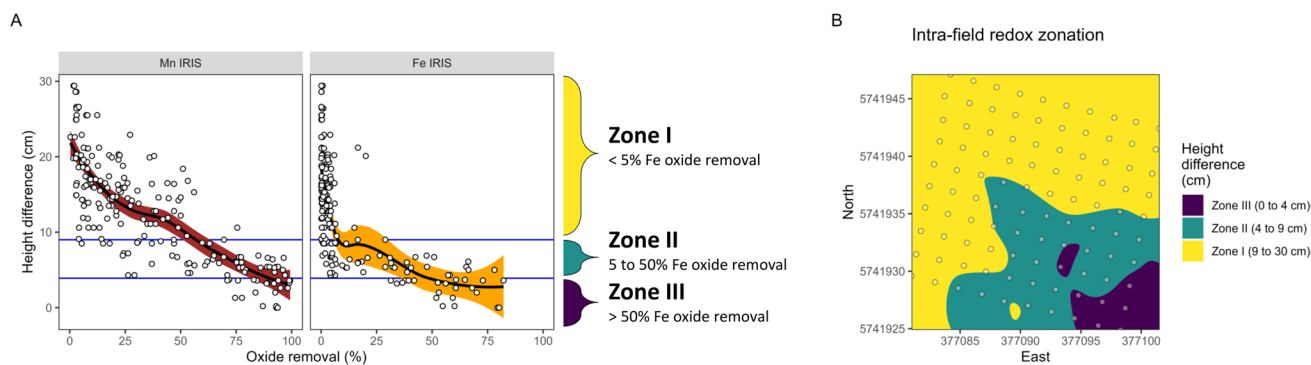
Fig. 3 Oxide removal from Mn and Fe IRIS plotted against altitude with the local regression trend (LOESS) through the data (**A**). Three distinctive zones were differentiated based upon Fe oxide removal: Zone I where Fe oxide removal is only marginal with < 5%, Zone II where Fe oxide removal is intermediate with 5 to 50%, and Zone III where Fe oxide removal is considerable with > 50%. The blue lines in (**A**) highlight the intersection of oxide loss and altitude within these zones. Finally, the differentiated redox zones (I to III) by consideration of these boundary altitudes are visualized for the study site (**B**)

curve between altitude and oxide removal from Fe IRIS zone I with < 5% oxide loss, zone II with 5 to 50% oxide loss, and zone III with > 50% oxide loss. Figure 3B shows the redox zonation that employs this classification. Most of the sampling points fall within zone I (62%) and zone II (29%), and only a little portion of the sampling points is within zone III (9%). In comparison, Mn oxide removal exceeded on average by a factor of three Fe oxide removal (Fig. 4A), and obviously, the standard deviation between duplicate Mn IRIS exceeded those of Fe IRIS (Fig. 4B). However, Mn IRIS did not reveal a clear trend with respect to the altitude because the standard deviation between duplicate films was in some occasions > 20% across zones I, II, and III. On the contrary, Fe IRIS were more equal when oxide removal is only marginal at the "drier" sites but more variable at the lowest terrain in zones II and III with up to 30% (Fig. 4B). Oxide removal along Fe IRIS is driven by Fe reducing conditions, whereas oxide removal along Mn IRIS is driven by Mn

reducing conditions and the presence of Fe^{2+} in soil solution. We assume that both factors lead to overall higher standard deviations along Mn IRIS contrary to Fe IRIS. For zones I and II, natural Fe oxides formed along Mn IRIS and were the driver and main factor for the dissolution of the synthetic and original Mn oxide coating with on average $85 \pm 17\%$ and $79 \pm 21\%$ contribution, whereas this contribution decreased to only $40 \pm 25\%$ in zone III (Fig. 4C).

3.3 Spatial analysis of soil properties and the soil redox status

The range of spatial dependence from Mn and Fe IRIS was 6.9 m for total Mn oxide removal, 4.2 m for natural Fe oxides, and largest with 7.9 m for Fe oxide removal (Fig. 5 A to C). pH distribution featured the lowest autocorrelation with a range of 3.1 m (Fig. 5D). A progressive decrease of spatial autocorrelation is equivalent to an increase in semivariance,
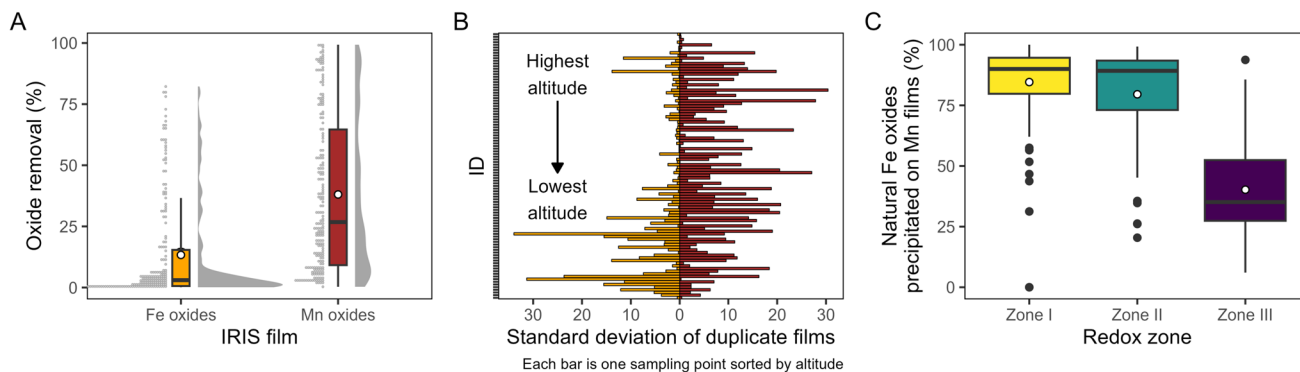
Fig. 4 Oxide removal of all Mn and Fe IRIS installed at the study site for a one-month period (each $n = 200$ films; **A**). The standard deviation of films installed in duplicate per sampling point (**n** = 100) is sorted by decreasing altitude for Mn and Fe IRIS and shown in (**B**). Finally, the coverage of natural Fe oxides precipitated along the Mn IRIS as a percentage ratio of the total Mn oxide removal for the differentiated redox zones (Zones I to III) is shown in (**C**)
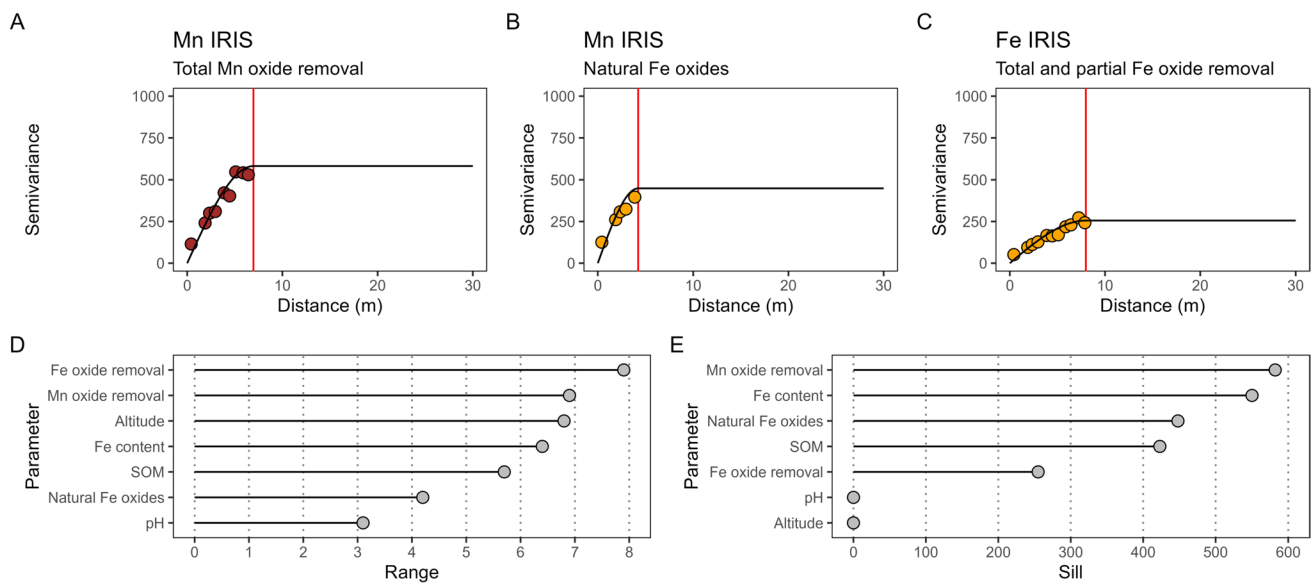
Fig. 5 Relevant spatial information of semivariograms to visualize redox maps featuring total oxide removal of Mn IRIS including areas of natural Fe oxides (**A**), percentage of precipitated natural Fe oxides from Mn IRIS (**B**), and oxide removal from Fe IRIS (**C**). The summary statistics of all created semivariograms including soil properties are displayed and sorted by decreasing range (**D**) and sill (**E**), respectively. In (**A**) to (**C**), data points are displayed until the range (red line). No nugget effect was observed

which was largest for the Fe content of the soil and oxide removal from Mn and Fe IRIS but very small for pH and altitude (Fig. 5E). Cross-validation of the created maps indicated an overall better performance for altitude and soil properties in comparison with information utilized to create redox maps. The interpolation procedures by OK to construct maps for altitude, pH, and SOC reflect a high degree of interpolation accuracy and reliability because the ASE and the RMSE were relatively equal (Table 2). Only for Fe content, ASE was smaller than RMSE indicating that the variability of prediction is underestimated. The scatter index (SI) for altitude was smallest with 0.1% and highlighted the best model performance to predict values of altitude at new locations in between the sampling points. However, while intra-field differentiation of decisive redox zones seems applicable from oxide loss of Mn and Fe IRIS, a SI of 35.9% for Mn oxide removal, 52.9% of natural Fe oxide formation, and up to 66% for Fe oxide removal from Fe IRIS make a prediction by OK less accurate (Fig. 4B and Table 2). This is an expression of variable depletion patterns along IRIS films in duplicate, even when being located in a few cm distance to each other.

4 Discussion

### 4.1 Redox zonation in intermittent wetlands

In the present study, an intra-field microrelief of less than 30 cm has a profound impact on soil properties and controls

Mn and Fe oxide reduction as evident from IRIS data included to construct redox maps (Fig. 2). Small field-scale redox zonation in intermittent wetlands featuring a microrelief is therefore an important feature and must be considered when pedogenetic information are retrieved. This is highlighted in the conceptualized scheme with focus on Mn and Fe oxide mineral (trans)formation at the study site (Fig. 6A). For instance, nested sampling of soil solution by suction cups in redox zone III with predominantly Fe^{III} reducing conditions will reveal high levels of soluble and reduced Mn^{2+} and Fe^{2+}. This is an indication of element transport via liquid phase and redistribution within the soil profile. On the contrary, sampling in redox zone I (predominantly aerobic with anoxic microsites) would potentially verify the absence of these reduced and mobile metal species in the

Table 2 Cross-validation of the created maps assessed by leave-one-out-method for the average standardized error (ASE), root mean square error (RMSE), and scatter index (SI)

Parameter	Unit	ASE	RMSE	SI (%)
Altitude	cm	0.03	0.03	0.1
pH	-	0.2	0.2	4.8
SOC	g kg^{-1}	1.4	1.5	17.5
Fe content	g kg^{-1}	16.1	20.0	21.3
Mn oxide removal (Mn IRIS)	%	13.5	13.7	35.9
Natural Fe oxides (Mn IRIS)	%	14.3	14.3	52.4
Fe oxide removal (Fe IRIS)	%	8.7	8.3	66.0
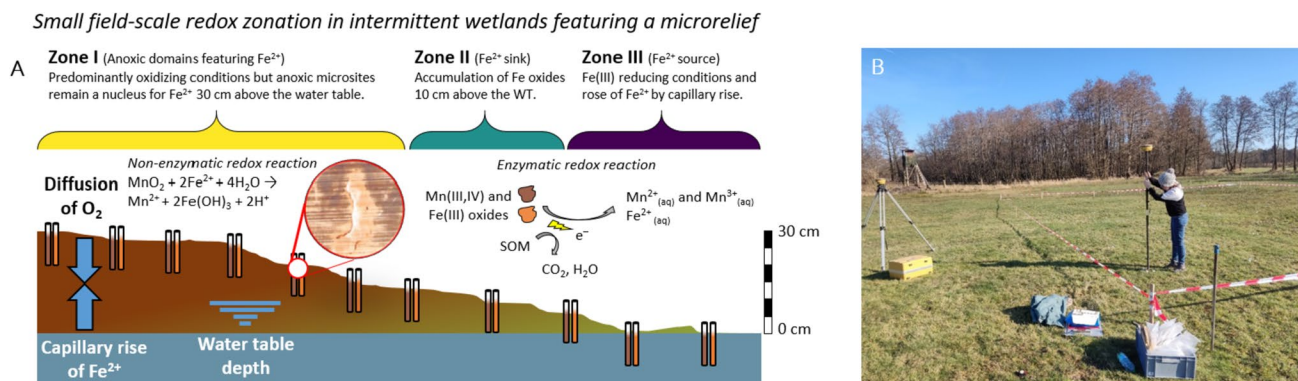
Fig. 6 Major findings summarized in a sketch from the lateral distribution of the study site featuring a microrelief (**A**) and image of the study site where Mn and Fe IRIS were installed with equipment to digitalize redox maps (**B**)

topsoil. Redox zonation at the field scale along with element redistribution has rarely been investigated with few examples (Fiedler et al. 2004). These features do not only occur due to glaciofluvial process such as in this study, but have also been studied in other parts of the world featuring permafrost soils. These soils sometimes have symmetrically formed ice wedge polygons from annual freeze–thaw cycles, which leads to a typical microrelief over time (Brown 1967). Element redistribution of Mn and Fe along hydraulic and redox gradients from the polygon center (i.e., microlow) towards the polygon rim (i.e., microhigh) has been observed by only 40 cm of differences in altitude (Fiedler et al. 2004). Kutzbach et al. (2004) have also shown for the same study site that small-scale spatial variability has impact on total CH_4 flux with 28.0 ± 5.4 mg m^{-2} d^{-1} at the depressed microlow and only 4.3 ± 0.8 mg m^{-2} d^{-1} at the microhigh.

Enhanced biogeochemical transformation of nutrients and pollutants is a key feature in wetlands around the world (Schlesinger and Emily 2013). As exemplified within this study, small geomorphic subunits (e.g., within a 20 × 20 m field) can feature localized zones of higher reactivity ("hot spots"). Explanation of these zones by static, physico-chemical properties might ultimately be too simplistic. This was shown within a virtual modeling experiment for a riparian wetland having a micro-topography with differently sized hollow and hummock structures (Frei et al. 2012). The model was capable to reproduce spatial variations in pore water concentrations of redox sensitive solutes (e.g., NO_3^-, Fe^{2+}, and SO_4^{2-}) and identify biogeochemical hotspots. A complex surface/subsurface interaction with the micro-topography alters in- and exfiltration solutes and hydrological controls either facilitate or suppress redox processes in in- and exfiltration areas (Frei et al. 2012). This certainly holds true for the redox zonation depicted for our study site, which is highly dynamic and not only depends on relatively static soil properties. The WT depth changes over time and can be up to 40 cm lower in the summer time (Dorau et al. 2016). Thereupon, variable

soil temperatures have a profound impact on the reductive Mn and Fe dissolution rates from Mn and Fe IRIS (Dorau et al. 2018b). Thus, measuring the oxide removal to a later stage during the year with drier conditions might reduce oxide removal due to the prevalence of oxic conditions. However, enhanced microbial activity due to elevated soil temperatures, which were as low as ~5 °C during the current monitoring period, would counterbalance reduced oxide removal to some extent. Overall, the current extent of redox zone I to III is not static because oxide removal from Mn and Fe IRIS is affected by external boundary conditions. In addition, the German soil classification system or the European Union do not have the concept of hydric soils that is applied in the USA for wetland resource management. According to the Hydric Soil Technical Standard, three out of five replicate Fe IRIS must demonstrate 30% oxide removal in a 15 cm zone that occur within 30 cm of the soil surface (Berkowitz et al. 2021). This regulatory threshold of 30% oxide loss would yield a different redox zonation as it was depicted within this study (Fig. S5). Thus, the redox zonation is not only affected by temporal dynamics (e.g., variable soil temperature and WT depths); it is also affected by regulatory definitions in terms of oxide removal.

4.2 Benefits of redox maps

Soil properties vary at small spatial scale, and because of this unknown spatial variability, experimentalists rely on a distinct number of replicates (Hofmann and Brus 2021; Weihermüller and Wessel-Bothe 2019). For instance, Weihermüller et al. (2006) demonstrated that soil solution obtained by suction cups to estimate solute transport has to be far greater than three replicates, even when evaluated within a homogeneous soil system. Small differences in altitude are not visible at first sight when inspecting a study site and deciding for an appropriate sampling strategy, not only but with specificity, to account for redox sensitive data and pedogenetic properties (Fig. 6B).

Representativeness of the samples taken in the field is a key to better understand the mechanistic relationship between controlling hydraulic factors (e.g., extent of the capillary fringe) and redox gradients (e.g., pH and SOC content) upon pedogenic processes such as mineral transformation and element redistribution. The question of how many replicates are sufficient to reliantly answer a specific question is very challenging but delineating a redox zonation upon certain spatial soil and study site information beneficial (Barczok et al. 2023; Tano et al. 2020). Decision-making tools can include a (i) digital elevation model, (ii) hydrologic information including the average WT depth, (iii) soil properties with impact on the onset of reduction (e.g., pH and SOC content), and (iv) supplemented by IRIS film oxide removal at distinct locations. This would greatly benefit to put the findings into perspective. While redox zone III makes up only 9% of the monitoring site, the majority (62%) is composed by redox zone I being more representative for the study area (Fig. 3B). Thus, if statements about the representativeness of the study site are needed for processes that prevail in the topsoil, experimentalists focusing on a specific research question should take the spatial extent of redox zonation into account. Delineation of reducing conditions in soils is of high importance for legislation and soil protection measures, e.g., according to the German Federal Soil Protection and Contaminated Sites Ordinance. Within this legislation, the transfer pathway "soil to plant" assumes an action value of 200 mg kg^{-1} arsenic (As) but only tolerates 50 mg kg^{-1} under temporarily reducing conditions (BBodSchV 1999). Lower tolerable As contents of 50 mg kg^{-1} are certainly valid for redox zone I to III–with reduction of pedogenic Fe(III) oxides–and the preconditions that the largest As fraction is associated with the Fe oxide pool of the soil (Mansfeldt and Overesch 2013). In this regard, uptake of contaminants such as and information from IRIS can also be valuable as a water management tool for rice farmers (Evans et al. 2021).

Digital soil maps (DSM) have been utilized to estimate the spatial distribution of soil classes and/or soil properties and can be applied at various scales ranging from the plot towards the country scale (Lagacherie et al. 2007). They are capable to generate solutions for the worldwide growing demand for high-resolution soil maps (Arrouays et al. 2020), since traditional surveys at scale of 1:25,000 are expensive and time-consuming (Behrens and Scholten 2006). In order to construct DSM, three approaches can be differentiated: (i) pedotransfer functions where one soil property (i.e., prevalence of a distinct redox class) is estimated by easier to measure soil properties and boundary conditions; (ii) geostatistical approaches such as kriging upon sampled and analyzed data, e.g., by IRIS; and finally (iii) state factor (clorpt) approaches upon regression, classification, or fuzzy-set theory approaches (summarized in Behrens and Scholten 2006). To adopt one of these three approaches in the future, to create larger scale redox maps is certainly a massive undertaking, because the distribution of soil classes and properties are relatively stable over time and, thus, are the representation of the map. Reducing conditions, however, are variable in space and time and the prevalence of decisive redox zones more difficult to map. Low-cost IRIS tools are certainly beneficial in this undertaking because most sensors determine the soil state of interest in a relatively small volume (e.g., soil water by tensiometer or E_H by Pt electrode measurements). The IRIS surface covers a significantly larger volume, and extrapolation to the field scale—classically the scale of interest in most soil research (Weihermüller and Wessel-Bothe 2019)—reduces a mismatch between measurement scale (i.e., dimension of the sensor) and scale of interest. The use of IRIS tools over Pt electrodes has some advantages: IRIS reflect the distribution of soil reducing conditions over the complete oxide-coated polymer surface that represents a continuum, whereas E_H readings by Pt electrodes reflect discrete point measurements (Dorau 2016). This renders Pt electrodes more susceptible to soil heterogeneity and leads to a misinterpretation of E_H data when the Pt tip dips into a soil aggregate assuming reducing conditions in an already aerobic soil environment. The susceptibility to microsite variability was underlined by the active surface area because electron transfer reactions occurred along 75 cm^2 at Mn and Fe IRIS compared with significantly smaller areas for conventional redox electrodes in the mm^2 or nm^2 range (Fig. 7).

4.3 Benefits and limitations of natural Fe oxide formation

Numerous studies have either specifically reported about natural Fe oxides formed along the Mn oxide coating from Mn IRIS or it is apparent from the images within the respective studies that these newly and in situ features have formed (Dorau and Mansfeldt 2015; Dorau and Mansfeldt 2016a, b; Evans et al. 2021; Rabenhorst et al. 2021). However, pedogenic Fe(III) oxides are certainly different to the mineralogical composition of synthetic Fe(III) oxides in terms of reducibility and reactivity. This is highlighted because synthetic oxide loss from Fe IRIS was virtually absent in redox zone I (Fig. 3 A and B), while reduction of pedogenic Fe oxides and the presence of Fe^{2+} in soil solution accounted for 80% of Mn oxide loss of Mn IRIS (Fig. 4C). Natural Fe oxides occur partly in microsites with only a small percentage area (e.g., Fig. 2A) or actually cover the complete surface of the previous applied Mn IRIS (e.g., Fig. 2C). Either way, the formation of natural Fe oxide needs a sufficient concentration of Fe^{2+} to facilitate a color change by displacement of the original Mn oxide coating.
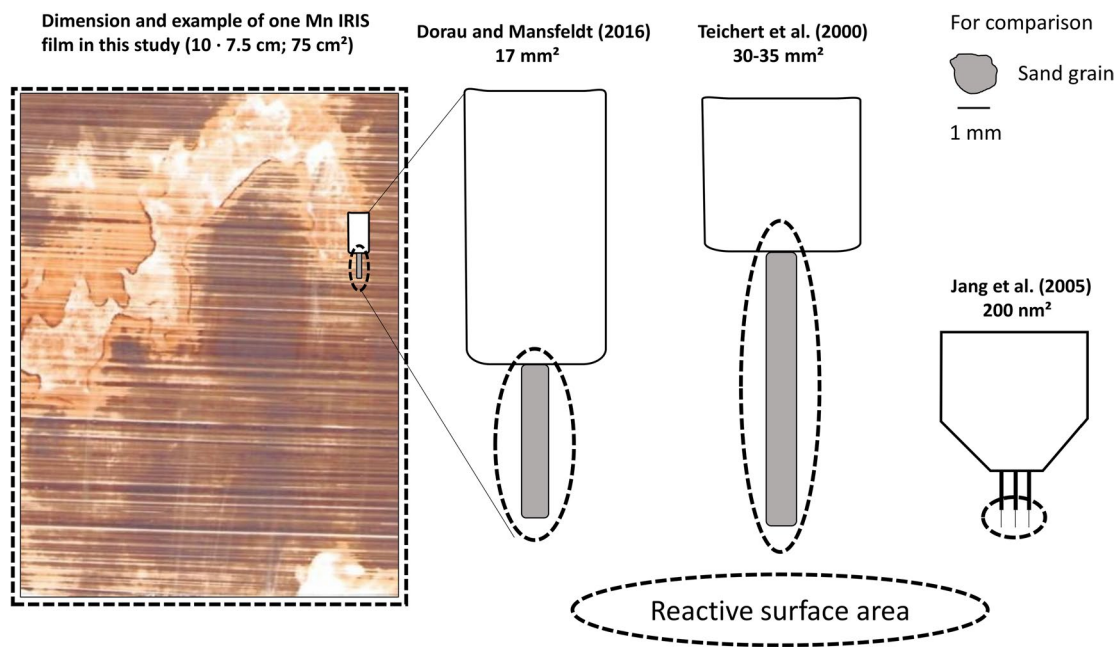
Fig. 7 Comparison of the reactive surface area for IRIS tools employed in this study and classical redox electrodes. The size of the platinum tipped wire, i.e., the reactive surface area, typically has dimensions between 17 and 35 mm² (Dorau and Mansfeldt 2016a; Teichert et al. 2000) but also miniaturized electrodes are available of only 200 nm² (Jang et al. 2005). A true scaling of the redox electrode is plotted inside the Mn IRIS from this study for comparison. The sand grain in the top right corner is the true scaling for the three types of redox electrodes

The pseudomorphic Fe oxides that form according to the reaction $MnO_2 + 2Fe^{2+} + 4H_2O \rightarrow Mn^{2+} + 2Fe(OH)_3 + 2H^+$ [Eq. 1] are likely first composed of short-range order Fe minerals (such as ferrihydrite or feroxyhyte). This was recently verified by a multitude of sophisticated methods such as µXRF and XANES spectra and fits (Limmer et al. 2023). The results were variable on small spatial scales (< 1 mm) with a predominance of ferrihydrite (30–90%) over lepidocrocite and goethite. Even though the mineralogical composition presumably varies significantly for this particular site, Mansfeldt et al. (2012) found for a detailed soil characterization by cryogenic ^{57}Fe Mössbauer spectroscopy from a Gleysol (Petrogleyic) pedon the following composition (~ 100 m distance to the monitoring plot): ferrihydrite (51%) over goethite (24%) in the Ah horizon while nanogoethite dominated the subsoil with 94% in the Bg and 86% in the CrBg horizon with minor composition of siderite (7%). At the very best, the mineralogical composition of the synthetic Fe oxide coating of Fe IRIS should resemble and mimic the prerequisites of pedogenic Fe oxides that can be found at a particular study site. However, in practice, this is virtually impossible to accomplish due to the expensive apparatuses using Mössbauer spectroscopy, and exclusive application of pure ferrihydrite will demonstrate poor adhesion and durability to the PVC surface (Rabenhorst and Burch 2006). Thereupon, it could be shown in a laboratory study

that crystal growth of ferrihydrite during coprecipitation in the presence of organic matter resulted in smaller crystal size and higher number of crystal defects, which explained the higher reactivity and reducibility in comparison with pure 2-line ferrihydrite (Eusterhues et al. 2014). Overall, this interesting finding of higher reducibility of pedogenic Fe oxides in comparison with synthetic Fe oxides from real in situ observations—a natural laboratory study—explains that natural Fe oxides are rich in structural defects. The collection of natural Fe oxides while avoiding chemical and physical artifacts during sampling is challenging but crucial for realistic analysis of mineral and other colloids in soil (Rennert et al. 2013). Avoidance of chemical and physical artifacts during sampling is one of the main benefits to characterize the mineralogical composition of neo-formed natural Fe oxides along Mn IRIS. This should be accomplished in more detail from a multitude of study sites in the future.

Despite many benefits, one of the main limitations while natural Fe oxides form is that the original purpose of Mn IRIS cannot be accomplished. Mn reduction is thermodynamically favorable with a free energy yield of 94.5 kJ mol^{-1} compared with 24.3 kJ mol^{-1} for Fe reduction (assuming CH_2O is the electron donor). In addition, soil bacteria show an enzymatic preference for Mn(III,IV) compared with Fe(III) (Lovley 1991; Zehnder and Stumm 1988). This was highlighted in this study by threefold enhanced oxide loss

from Mn over Fe IRIS or previously under controlled conditions (Dorau and Mansfeldt 2015). Preferential dissolution of the Mn oxide coating of Mn IRIS without any simultaneously removal of Fe oxides of Fe IRIS highlights weakly reducing conditions, which can be deduced at E_H 300 to 100 mV at pH 7 according to Reddy and DeLaune (2008). This redox class is presumably of higher ecological relevance because nitrogen transformation from NO_3^- to N_2O or N_2 or via ammonification to NH_4^+ takes place at this E_H range (Schlesinger and Emily 2013). The simultaneous onset of the occurrence of Mn^{2+} and Fe^{2+} in soil solution arguably raises the question: How relevant is the spatiotemporal prevalence of weakly reducing conditions in soil? Exclusive reduction of Mn oxides without precipitation of natural Fe oxides occurred only in redox zone III within the study site (Figs. 2D, 3B). This was the zone where also synthetic Fe oxides were predominantly reduced and implies that both Mn^{2+} and Fe^{2+} can be found in soil solution. To clarify and contribute to this debate, it would be valuable to calculate and analyze in future studies ratios of Mn oxide loss due to natural Fe oxides (Mn_{Fe-nat}) divided by total oxide loss of Mn IRIS (Mn_{total}). Only low ratios (e.g., $< 0.1 \frac{Mn_{Fe-nat}}{Mn_{total}}$) that occur without oxide loss from Fe IRIS are indicative for predominance of weakly reducing soil conditions.

5 Conclusions

In this study, we presented an approach to create redox maps by installation of Mn and Fe oxide-coated IRIS films and distinguish from oxide removal a decisive redox zonation. This is particularly helpful to localize zones of higher reactivity ("hot spots") due to the presence of a micro-topography or variable soil properties. Mn(III,IV) and Fe(III) mineral transformation due to electron transfer reactions is primarily driven at the microscale along tiny biogeochemical interfaces. However, the large reactive surface area of IRIS can circumvent problems associated with misclassification of the soil redox status using redox electrodes, which are susceptible to soil spatial variability. IRIS can deliver both information: microscale features such as neo-formed natural Fe oxides that can be observed and investigated in more detail ($<$ mm to cm) and redox zonation due to micro-topography driven plot features by incorporating geo-referenced oxide loss from IRIS at the plot scale (tens to hundreds of meters; Fig. 6). Synthetic Fe oxide removal from Fe IRIS was strictly bound to the WT surface. Contrary, natural Fe oxides formed even 30 cm above the WT within the capillary fringe, highlighting a substantial reductive dissolution of pedogenic Fe(III) oxides within anoxic microsites to deliver Fe^{2+} to the synthetic Mn oxide coating from Mn IRIS. In terms of decision-making for representative redox-sensitive

soil samples: Field designs and monitoring protocols can potentially be elucidated by incorporating oxide loss from IRIS to determine the degree of intra-field variability. This would be supportive as a low-cost alternative to suction cups or at least in conjunction with suction cups, the latter more expensive and tedious in maintenance, to acquire and analyze soil solution for redox-sensitive elements.

Availability of data and materials Data can be accessed from the authors by reasonable request.

Declarations

Ethics approval Not applicable.

Consent to participate All authors agreed to participate in this research study.

Consent for publication The authors warrant that the work has not been published before and is not under consideration by another publisher.

Conflict of interest The authors declare no conflict of interests.

References

Arrouays D, McBratney A, Bouma J, Libohova Z, Richer-de-Forges AC, Morgan CLS, Roudier P, Poggio L, Mulder VL (2020) Impressions of digital soil maps: The good, the not so good, and

making them ever better. Geoderma Reg 20:e00255. https://doi.org/10.1016/j.geodrs.2020.e00255

Banning A, Coldewey WG, Goebel P (2009) A procedure to identify natural arsenic sources, applied in an affected area in North Rhine-Westphalia, Germany. Environ Geol 57:775–787. https://doi.org/10.1007/s00254-008-1355-4

Barczok M, Smith C, Di Domenico N, Kinsman-Costello L, Herndon E (2023): Variability in soil redox response to seasonal flooding in a vernal pond. Front Environ Sci 11 https://doi.org/10.3389/fenvs.2023.1114814

Barthelme S (2021) imager: Image Processing Library Based on 'CImg'. (version 0.42.7)

BBodSchV (1999) Bundes-Bodenschutz- und Altlastenverordnung vom 12. Juli 1999 BGBl. I S. 1554), die zuletzt durch Artikel 102 der Verordnung vom 31. August 2015 (BGBl. I S. 1474) geändert worden ist

Behrens T, Scholten T (2006) Digital soil mapping in Germany – a review. J Plant Nutr Soil Sci 169:434–443. https://doi.org/10.1002/jpln.200521962

Berkowitz JF, Vepraskas MJ, Vaughan KL, Vasilas LM (2021) Development and application of the hydric soil technical standard. Soil Sci Soc Am J 85:469–487. https://doi.org/10.1002/saj2.20202

Brown J (1967) Tundra soils formed over ice wedges, Northern Alaska. Soil Sci Soc Am J 31:686–691. https://doi.org/10.2136/sssaj1967.03615995003100050022x

DeLaune RD, Reddy KR (2005) Redox potential. In: Hillel D (ed) Encyclopedia of soils in the environment. Academic Press, San Diego, CA, USA, pp 366–371

Dorau K, Mansfeldt T (2015) Manganese-oxide-coated redox bars as an indicator of reducing conditions in soils. J Environ Qual 44:696–703. https://doi.org/10.2134/jeq2014.03.0140

Dorau K (2016) Monitoring of reducing conditions in soils and implications for biogeochemical processes. Dissertation, University of Cologne

Dorau K, Eickmeier M, Mansfeldt T (2016) Comparison of manganese and iron oxide-coated redox bars for characterization of the redox status in wetland soils. Wetlands 36:133–144. https://doi.org/10.1007/s13157-015-0724-5

Dorau K, Mansfeldt T (2016a) Comparison of redox potential dynamics in a diked marsh soil: 1990 to 1993 versus 2011 to 2014. J Plant Nutr Soil Sci 179:641–651. https://doi.org/10.1002/jpln.201600060

Dorau K, Mansfeldt T (2016b) Manganese and iron oxide-coated redox bars as a tool to in situ study the element sorption in wet soils. J Soil Sediment 16:976–986. https://doi.org/10.1007/s11368-015-1300-6

Dorau K, Luster J, Mansfeldt T (2018a) Soil aeration: the relation between air-filled pore volume and redox potential. Eur J Soil Sci 69:1035–1043. https://doi.org/10.1111/ejss.12717

Dorau K, Papenfuß S, Mansfeldt T (2018b) Temperature-dependent oxide removal from manganese- and iron oxide-coated soil redox bars. J Soil Sediment 18:680–687. https://doi.org/10.1007/s11368-017-1812-3

Dorau K, Wessel-Bothe S, Milbert G, Schrey HP, Elhaus D, Mansfeldt T (2020) Climate change and redoximorphosis in a soil with stagnic properties. CATENA 190:104528. https://doi.org/10.1016/j.catena.2020.104528

Dorau K, Uteau D, Hövels MP, Peth S, Mansfeldt T (2021) Soil aeration and redox potential as function of pore connectivity unravelled by X-ray microtomography imaging. Eur J Soil Sci 73:1–10. https://doi.org/10.1111/ejss.13165

Dorau K, Uteau D, Maisch M, Kappler A, Peth S, Mansfeldt T (2023) Redoxtrons – An experimental system to study redox processes within the capillary fringe. Eur J Soil Sci 74:e13347. https://doi.org/10.1111/ejss.13347

Eusterhues K, Hädrich A, Neidhardt J, Küsel K, Keller TF, Jandt KD, Totsche KU (2014) Reduction of ferrihydrite with adsorbed and coprecipitated organic matter: microbial reduction by Geobacter bremensis vs. abiotic reduction by Na-dithionite. Biogeosciences 11:4953–4966. https://doi.org/10.5194/bg-11-4953-2014

Evans AE, Limmer MA, Seyfferth AL (2021) Indicator of redox in soil (IRIS) films as a water management tool for rice farmers. J Environ Manage 294:112920. https://doi.org/10.1016/j.jenvman.2021.112920

Fiedler S, Wagner D, Kutzbach L, Pfeiffer E-M (2004) Element redistribution along hydraulic and redox gradients of low-centered polygons, Lena Delta, Northern Siberia. Soil Sci Soc Am J 68:1002–1011. https://doi.org/10.2136/sssaj2004.1002

Frei S, Knorr KH, Peiffer S, Fleckenstein JH (2012) Surface microtopography causes hot spots of biogeochemical activity in wetland systems: a virtual modeling experiment. J Geophys Res Biogeosci 117:1–18. https://doi.org/10.1029/2012JG002012

Gräler B, Pebesma EJ, Heuvelink GBM (2016) Spatio-temporal interpolation using gstat. R Journal 8:204–218. https://doi.org/10.32614/RJ-2016-014

Hiemstra PH, Pebesma EJ, Twenhöfel CJW, Heuvelink GBM (2009) Real-time automatic interpolation of ambient gamma dose rates from the Dutch radioactivity monitoring network. Comput Geosci 35:1711–1721. https://doi.org/10.1016/j.cageo.2008.10.011

Hindersmann I, Mansfeldt T (2014) Trace element solubility in a multimetal-contaminated soil as affected by redox conditions. Water Air Soil Pollut 225:1–20. https://doi.org/10.1007/s11270-014-2158-8

Hofman SCK, Brus DJ (2021) How many sampling points are needed to estimate the mean nitrate-N content of agricultural fields? A geostatistical simulation approach with uncertain variograms. Geoderma 385:114816. https://doi.org/10.1016/j.geoderma.2020.114816

Jang A, Lee JH, Bhadri PR, Kumar SA, Timmons W, Beyette FR Jr, Papautsky I, Bishop PL (2005) Miniaturized redox potential probe for in situ environmental monitoring. Environ Sci Technol 39:6191–6197. https://doi.org/10.1021/es050377a

Jenkinson BJ, Franzmeier DP (2006) Development and evaluation of iron-coated tubes that indicate reduction in soils. Soil Sci Soc Am J 70:183–191. https://doi.org/10.2136/sssaj2004.0323

Kaur L, Rishi M (2018) Integrated geospatial, geostatistical, and remote-sensing approach to estimate groundwater level in North-western India. Environ Earth Sci 77:786. https://doi.org/10.1007/s12665-018-7971-8

Kisi O, Shiri J, Tombul M (2013) Modeling rainfall-runoff process using soft computing techniques. Comput Geosci 51:108–117. https://doi.org/10.1016/j.cageo.2012.07.001

Kutzbach L, Wagner D, Pfeiffer E-M (2004) Effect of microrelief and vegetation on methane emission from wet polygonal tundra, Lena Delta, Northern Siberia. Biogeochem 69:341–362. https://doi.org/10.1023/B:BIOG.0000031053.81520.db

Lagacherie P, McBratney AB, Voltz M (2007) Digital soil mapping: an introductory perspective. Developments in soil science, Vol. 31. Elsevier, Amsterdam, The Netherlands

Limmer MA, Linam FA, Evans AE, Seyfferth AL (2023) Unraveling the mechanisms of Fe oxidation and Mn reduction on Mn indicators of reduction in soil (IRIS) films. Environ Sci Technol 57:6530–6539. https://doi.org/10.1021/acs.est.3c00161

Lovley DR (1991) Dissimilatory Fe(III) and Mn(IV) reduction. Microbiol Rev 55:259–287. https://doi.org/10.1016/S0065-2911(04)49005-5

Mansfeldt T, Schuth S, Häusler W, Wagner F, Kaufhold S, Overesch M (2012) Iron oxide mineralogy and stable iron isotope composition in a Gleysol with petrogleyic properties. J Soil Sediment 12:97–114. https://doi.org/10.1007/s11368-011-0402-z

Mansfeldt T, Overesch M (2013) Arsenic mobility and speciation in a gleysol with petrogleyic properties: a field and laboratory approach. J Environ Qual 42:1130–1141. https://doi.org/10.2134/jeq2012.0225

Mehra OP, Jackson ML (1960) Iron oxide removal from soils and clays by a dithionite-citrate system buffered with sodium bicarbonate. Clay Clay Miner 7:317–327. https://doi.org/10.1016/B978-0-08-009235-5.50026-7

Pebesma E (2018) Simple features for R: standardized support for spatial vector data. R Journal 10:439–446. https://doi.org/10.32614/RJ-2018-009

Ponnamperuma FN (1972) The chemistry of submerged soils. In: Brady NC (ed) Advances in Agronomy. Academic Press, San Diego, CA, USA, pp 29–96

Rabenhorst M (2018) A system for making and deploying oxide-coated plastic films for environmental assessment of soils. Soil Sci Soc Am J 82:1301–1307. https://doi.org/10.2136/sssaj2018.05.0178

Rabenhorst MC, Burch SN (2006) Synthetic iron oxides as an indicator of reduction in soils (IRIS). Soil Sci Soc Am J 70:1227–1236. https://doi.org/10.2136/sssaj2005.0354

Rabenhorst MC, Persing KA (2017) A synthesized manganese oxide for easily making durable manganese-coated IRIS tubes. Soil Sci Soc Am J 81:233–239. https://doi.org/10.2136/sssaj2016.10.0348n

Rabenhorst MC, Drohan PJ, Galbraith JM, Moorberg C, Spokas L, Stolt MH, Thompson JA, Turk J, Vasilas BL, Vaughan KL (2021) Manganese-coated IRIS to document reducing soil conditions. Soil Sci Soc Am J 85:2201–2209. https://doi.org/10.1002/saj2.20301

Reddy KR, DeLaune RD (2008) Biogeochemistry of wetlands - science and applications. CRC Press, Boca Raton, FL, USA. https://doi.org/10.1201/9780203491454

Rennert T, Mueller CW, Mansfeldt T, Lugmeier J (2013) Collecting in situ precipitated iron oxides in their natural soil environment. J Plant Nutr Soil Sci 176:497–499. https://doi.org/10.1002/jpln.201300184

Rohe L, Apelt B, Vogel HJ, Well R, Wu GM, Schlüter S (2021) Denitrification in soil as a function of oxygen availability at the microscale. Biogeosciences 18:1185–1201. https://doi.org/10.5194/bg-18-1185-2021

Sapkota Y, Duball C, Vaughan K, Rabenhorst MC, Berkowitz JF (2022) Indicator of Reduction in Soil (IRIS) devices: a review. Sci Total Environ 852:158419. https://doi.org/10.1016/j.scitotenv.2022.158419

Schlesinger WH, Emily SB (2013) Biogeochemistry: an analysis of global change, 3rd edn. Academic Press, Amsterdam, Netherlands. https://doi.org/10.1016/C2010-0-66291-2

Schroeder H, Fabricius A-L, Ecker D, Ternes TA, Duester L (2017) Metal(loid) speciation and size fractionation in sediment pore water depth profiles examined with a new meso profiling system. Chemosphere 179:185–193. https://doi.org/10.1016/j.chemosphere.2017.03.080

Schwertmann U (1964) Differenzierung der Eisenoxide des Bodens durch Extraktion mit Ammoniumoxalat-Lösung. Z Pflanzr Düng Bodenk 105:194–202. https://doi.org/10.1002/jpln.3591050303

Schwyter A (2020) Climatic influence on wetland biogeochemistry and function using an elevational sequence in the Rocky Mountains, WY. MS thesis, University of Wyoming

Stiles CA, Dunkinson ET, Ping CL, Kidd J (2010) Initial field installation of manganese indicators of reduction in soils, Brooks Range, Alaska. Soil Sur Hor 51:102–107. https://doi.org/10.2136/sh2010.4.0102

Tano BF, Brou CY, Dossou-Yovo ER, Saito K, Futakuchi K, Wopereis MCS, Husson O (2020) Spatial and temporal variability of soil redox potential, ph and electrical conductivity across a toposequence in the savanna of west africa. agronomy 10:1787. https://doi.org/10.3390/agronomy10111787

Teichert A, Böttcher J, Duijnisveld WHM (2000) Redox measurements as a qualitative indicator of spatial and temporal variability of redox state in a sandy forest soil. In: Schüring J, Schulz HD, Fischer WR, Böttcher J , Duijnisveld WHM (Editors), Redox: fundamentals, processes, and applications. Springer-Verlag Berlin, Heidelberg

Vogel H-J, Balseiro-Romero M, Kravchenko A, Otten W, Pot V, Schlüter S, Weller U, Baveye PC (2022) A holistic perspective on soil architecture is needed as a key to soil functions. Eur J Soil Sci 73:e13152. https://doi.org/10.1111/ejss.13152

Weihermüller L, Kasteel R, Vereecken H (2006) Soil heterogeneity effects on solute breakthrough sampled with suction cups: numerical simulations. Vadose Zone Journal 5:886–893. https://doi.org/10.2136/vzj2005.0105

Weihermüller L, Wessel-Bothe S (2019) Field measurements methods in soil science. Borntraeger Science Publishers Stuttgart, Germany, Gebr

Whitfield M (1974) Thermodynamic limitations on the use of the platinum electrode in E_H measurements. Limnol Oceanogr 19:857–865. https://doi.org/10.4319/lo.1974.19.5.0857

Wickham H et al (2019) Welcome to the Tidyverse. Journal of Open Source Software 4:1686. https://doi.org/10.21105/joss.01686

Yu KW, Patrick WH (2004) Redox window with minimum global warming potential contribution from rice soils. Soil Sci Soc Am J 68:2086–2091. https://doi.org/10.2136/sssaj2004.2086

Zausig J, Stepniewski W, Horn R (1993) Oxygen concentration and redox potential gradients in unsaturated model soil aggregates. Soil Sci Soc Am J 57:908–916. https://doi.org/10.2136/sssaj1993.03615995005700040005x

Zehnder AJB, Stumm W (1988) Geochemistry and biogeochemistry of anaerobic habitats. In: Zehnder AJB (Editor), Biology of anaerobic microorganisms. John Wiley & Sons, New York, NY, USA, pp. 1–38